Carbon 139 (2018) 445–458

Contents lists available at ScienceDirect

Carbon

journal homepage: www.elsevier.com/locate/carbon

19-Fold thermal conductivity increase of carbon nanotube bundles toward high-end thermal design applications

Yangsu Xie [a, b], Tianyu Wang [b], Bowen Zhu [b], Chaoyi Yan [a], Peixin Zhang [a], Xinwei Wang [b, *], Gyula Eres [c, **]

[a] College of Chemistry and Environmental Engineering, Shenzhen University, Shenzhen, 518055, Guangdong, PR China
[b] Department of Mechanical Engineering, 2025 Black Engineering Building, Iowa State University, Ames, IA, 50011, USA
[c] Oak Ridge National Laboratory, Materials Science and Technology Division, Bldg 4100, MS 6056, Oak Ridge, TN, 37831, USA

ARTICLE INFO

Article history:
Received 27 April 2018
Accepted 4 July 2018
Available online 5 July 2018

ABSTRACT

In high temperature annealing of carbon nanotube (CNTs) bundles for structure and thermal conductivity (κ) improvement, the statistical errors from sample-wide structure variation and sample transfer/preparation significantly overshadows the understanding of structure-κ correlation and change. In this work, the sequential process of current-induced thermal annealing (CITA) on improving the structure, electrical and thermal conductivities of chemical vapor deposition grown CNT bundles is studied for the first time. Our in-situ κ measurement using the transient electro-thermal technique uncovers the conjugated dynamic electrical, thermal, and structural properties. The electrical resistance and thermal diffusivity evolution of CNT bundles during CITA is studied. The thermal diffusivity and κ before and after CITA are measured from room temperature down to 10 K to uncover the reduction of defect density and enhancement of inter-tube connection strength after CITA. Our micro-Raman spectroscopy study from the most annealed region to the non-annealed region reveals significantly improved order in sp^2 bonding carbon structure and reduced defects along the sample length. The resulting κ has 5–19 times increase at the most annealed region of CNT bundles. The intrinsic κ of CNT walls against the annealing temperature is also determined, which reaches a level as high as 754 W/m·K after CITA.

1. Introduction

Carbon nanotubes (CNTs) are allotropes of carbon with a cylindrical nanostructure. Considerable interests have been attracted by its exceptional properties. Various promising potential applications of CNTs in nanostructured engineering have been reported [1–7]. CNTs have exceptionally high young's modulus (Y = 1.8 TPa) [8] and tensile strength (as high as 0.15 TPa) [9,10], high electronic mobility (tens of thousands of $cm^2\ V^{-1}\ s^{-1}$ at room temperature has been reported) [11,12], and high thermal conductivity [13]. Among those excellent properties, the high thermal conductivity (κ) is of significant importance for CNTs' application. Very high κ values of individual CNTs in the order of 3000 W/m·K at room temperature (RT) were reported [14–16]. 3000 and 2000 W/m•K have been reported for multi-walled CNT [17] and single-walled CNT [16] respectively, which is comparable to κ of diamond and much higher than that of pure metals. However, for bulk forms of CNTs, the thermal conductivities are much lower due to the high structure defects and large inter-tube thermal contact resistance. Bauer et al. measured κ of vertically aligned CNT arrays to be only 49–79 W/m·K [18]. Other works reported even lower values (<25 W/m·K) [19,20]. κ of MWCNT films were reported to be about 15 W/m K by using a photothermal reflectance technique [21]. For SWCNTs mats, κ was measured to be about 35 W/m•K according to Hone et al. [22].

Chemical vapor deposition (CVD) is a dominant method for high-volume CNT production. By producing in large quantity, using low-cost feedstock, increasing yield and reducing energy consumption, CNT price has been substantially reduced. However, the large-scale CVD method always yields CNTs with contaminants and lattice defects. The existence of defects and impurities including nanoparticles, amorphous carbon and multi-shell carbon nanocapsules, significantly inhibits the electrical and thermal properties of CNTs. CNTs often form bundles, which are macroscopic assemblies of axially aligned CNTs. Past work reported that CNT

* Corresponding author.
** Corresponding author.
E-mail addresses: xwang3@iastate.edu (X. Wang), eresg@ornl.gov (G. Eres).

https://doi.org/10.1016/j.carbon.2018.07.009
0008-6223/

arranged in regular arrays of bundles is a promising candidate for devices requiring high-intensity electron beams from field emission sources [23]. SWCNT bundle interconnects showed significant advantages over Cu in terms of performance, power dissipation, as well as thermal management/reliability [24]. Due to the existence of defects and impurities, tube-to-tube thermal contact resistance, and low density, κ of CNT bundles was reported to be two to three orders of magnitude lower than that of individual CNTs [20]. There is considerable room for improvement of thermal conductivity by reducing defects and impurities and improving interconnection strength in CNT bundles.

High-yield purification to separate and eliminate impurities and defects in CVD grown CNTs is undergoing intense study. Among various purification methods, high temperature annealing (between 800 °C and 3000 °C) under vacuum environment is reported to be especially effective and simple to remove microstructural defects and impurities in CNTs [25–29]. In order to find the optimum conditions for thermal annealing, extensive work has been conducted to characterize structure change and understand the kinetic thermal properties evolution during thermal annealing. Kim et al. studied sequential structural changes of bundles of double-walled CNTs (DWNTs) as a function of heat treatment temperature for the first time by using Raman spectroscopy and high-resolution transmission electron microscopy (HRTEM) [30]. Jin et al. reported that the thermal conductivity of CNTs are sensitive to sample crystallinity that was greatly improved by high-temperature annealing [31]. However, it is still challenging to study sequential evolution of thermal and electrical properties of CNTs during annealing process. The challenges are summarized as following: first, the CNT material could be contaminated or damaged during the process of transferring sample to the experimental set-up for thermal characterization. In addition, it is too difficult to control the quality variation among different samples to make cogent thermal properties comparison. No comprehensive work about the sequential thermal and electrical evolution of CNTs during thermal annealing process has been reported to our best knowledge.

Like direct high-temperature annealing, electric current-induced thermal annealing (CITA) is simpler yet highly effective. The effect of large current on conductor includes electromigration and joule heating [32]. It has been reported that electromigration has an insignificant effect on the resistance or morphology of CNTs [33]. However, CITA is still different from high temperature annealing in some respects. For inhomogeneous structures, electrical resistance distribution is nonuniform in space. When a large current is applied, regions with larger electrical resistance will experience much higher density of joule heating power. Thus, these regions are easily burnt or melt, which results in changes in the inner structure. Past works showed that electric current has a positive effect on the structure of carbon materials including graphene and graphite [34,35]. Moser et al. introduced current-induced cleaning of graphene at low temperatures inside a cryostat. By applying an electrical current through graphene device of microns width, the ultrahigh current density was able to effectively remove contaminations absorbed on surface of graphene [32]. Furthermore, applying current is very useful in maintaining the wall number and diameter of SWCNTs during high temperature annealing [36]. Because of the structure improvement, thermal and electrical properties of CNT materials are also enhanced, which is significant for their application in electronic, solar energy storage and other related areas. Bolotin et al. reported that current-induced annealing resulted in a significant enhancement of electrical transport in suspended single-layered graphene [37]. However, to our best knowledge, no work has been done about the thermal conductivity/diffusivity enhancement by CITA.

Herein, we demonstrate how this electric current-induced thermal annealing can be combined with the transient electrothermal technique (TET) to study the sequential thermal and electrical properties evolution of CNTs materials during annealing. The TET technique is a fast, simple and robust method developed in our lab for characterizing thermal properties of solid materials [38–42]. By using the same experimental set-up for annealing and thermal characterization, this method avoids the errors resulted from the sample to sample quality variation as well as contamination and damage caused by sample transferring process. For comparison, traditional high temperature annealing anneals a group of samples at different temperatures in furnaces followed by thermal characterization. The uncertainty caused by quality variation among samples and samples contamination during transferring process could be very large, which overshadows the annealing effect on structure and physical properties.

In this work, the CITA effects on improving the electrical and thermal properties of CNT bundles are reported. The structure change of CNT bundles from thermal transport aspect is studied by measuring the temperature-dependent thermal diffusivity and conductivity of the same sample before and after CITA. Raman spectroscopy is conducted to investigate the annealing effect on improving the structure of material and reducing impurities. The temperature distribution along the length direction of a single CNT bundle during CITA is evaluated using finite difference modeling. The different annealing levels at different positions of sample is harnessed for studying and comparing the temperature effect, which significantly reduces the deviation from sample quality variation. The resulting improvement of localized thermal conductivity and intrinsic thermal conductivity of CNT walls against annealing temperature during CITA process is also presented.

2. Synthesis and structure characterization

The vertically aligned multi-walled carbon nanotube (MWCNT) bundles arrays on a Si (100) wafer are synthesized by chemical vapor deposition (CVD) process in a quartz tube furnace. Briefly, a two-layer metal catalyst film with 10 nm of Al and 1 nm of Fe is used. 9 cm^3/min at STP (SCCM) of acetylene, 100 SCCM of hydrogen, 250 SCCM of helium, and 4 mg/h of thermally evaporated ferrocene, $Fe(C_5H_5)_2$ is introduced as feedstock for the CNT growth. Ferrocene enhances the efficiency of the pre-deposited catalyst film and postpones growth termination, resulting in higher CNT growth rates and thicker CNT films. The diameter of the bundle is controlled by using a patterned catalyst area. MWCNT bundles with bundle diameter of about 200 μm are harvested from a large area sample for thermal properties measurements. The details of the synthesis process can be found in the literature [43].

Fig. 1 presents the morphology and structure of a single CNT bundle sample. Figure (a)- (b) are SEM images with different magnification from 500× to 15000×. The CNT bundles sample presents a cylinder-like shape. Hundreds of thousands of CNTs form a bundle by aligning along the axial direction. Under higher magnification, coil-like CNTs can be seen. The coil-like CNT morphologies are driven by the competing factors of collective growth and spatial constraints during CVD process [44]. The diameter and wall thickness of individual CNT in the bundle are characterized using transmission electron microscopy (TEM). Fig. 1 (c)-(d) are two of the TEM images of the MWCNTs in the bundle. TEM reveals that the CNT bundles consist of MWCNTs with typical outer diameter from 18 to 25 nm. The wall thickness ranges from 15 to 22 layers. The wall of the MWCNT is not smooth. As indicated by the yellow arrows, amorphous region and defects are observed along the walls of CNTs. Wall thickness also varies along the axial direction.

Raman result of CNT bundles is obtained under 20× objective by

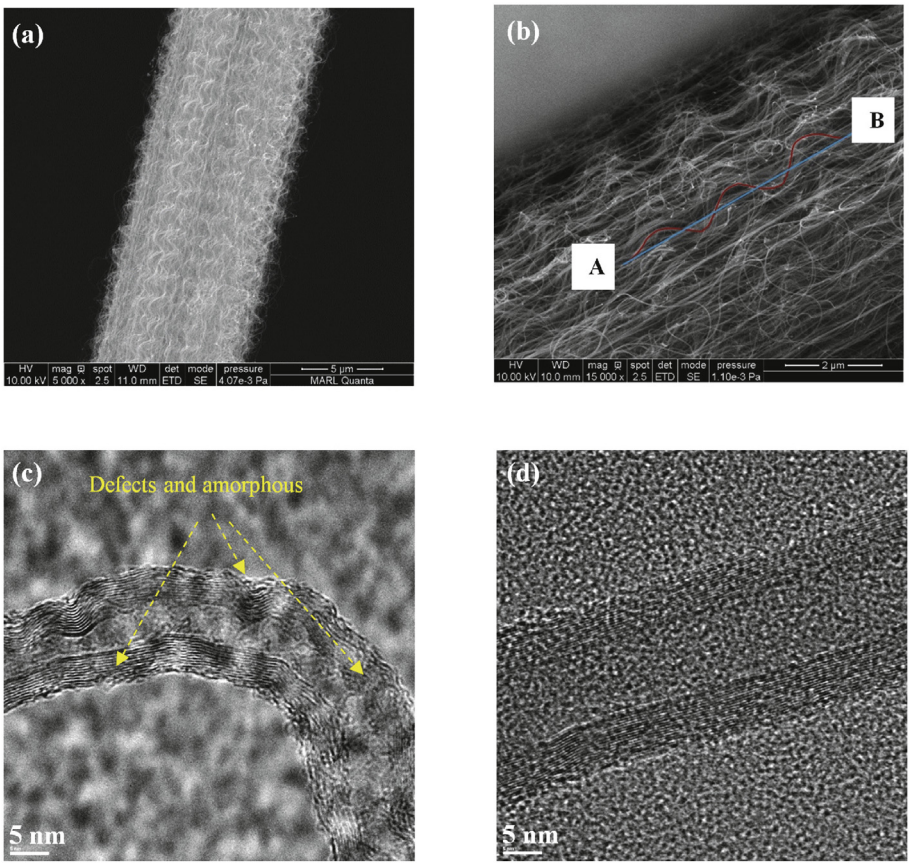

Fig. 1. Morphology and structure characterization of CNT bundles. (a)–(b) SEM images of the CNT bundles under ×500 and ×15000 magnifications. (c)–(d) TEM images. The yellow arrows indicate the amorphous region. (e) Raman spectrum. (f) XRD spectrum. (g) The X-ray photoelectron spectra. In the insets are the deconvoluted spectrums for O 1s and C 1s. (To be continued). (A colour version of this figure can be viewed online.)

using 532 nm laser excitation with 6 s integration time (Olympus BX51). The power of laser is 4.98 mW. The result is presented in Fig. 1 (e). Three pronounced peaks are observed which correspond to the D peak, G peak and 2D peak respectively. The G peak (1583.0 cm^{-1}) is from stretching of the C-C bond in graphitic materials, which is usually assigned to zone center phonons of E_{2g} symmetry. Its intensity reflects the degree of carbonization [45]. Near the G band, there is an additional shoulder peak at about 1618 cm^{-1}, called D′ band. The D′ band is a unique Raman band for MWCNTs, which also originates from disorder, defects or ion intercalation between the graphitic walls [46]. The D peak at around 1348.1 cm^{-1} involves the resonantly enhanced scattering of electrons via phonon emission by defects or sidewalls that breaks the basic symmetry of the graphene plane [47], which can be used as an indicative of structural disorder from amorphous carbon and other defects. The integrated intensity ratio between the D band and G band shows a value of ~0.86, which is smaller than the previously reported value for CVD grown MWCNTs and graphitized MWCNTs [46]. The 2D peak (2689.5 cm^{-1}) is activated by double resonance processes [48], which indicates the long-range order. These results reveal the fair graphitic structure and the existence of defects in the CNT bundles.

X-ray diffraction (XRD) is performed to obtain detailed structural and phase information about the CNT bundles. Three peaks are observed in the XRD profile presented in Fig. 1(f). The strong and sharp (002) peak at around 25.8° corresponds to the interplanar spacing of 0.34 nm, which is very close to that of pure graphite (0.335 nm). This result indicates that the inter-wall impurities are rare. The other two diffraction peaks at the angles 2θ of 42.8° and 53.4° are indexed to the (100) and (004) reflections. The (100) peak gives a crystallite size of 27.5 nm (crystallite size along axial-direction of a CNT). The crystallite size is calculated according to the Scherrer Equation: $B=K\lambda/(L\cos\theta)$, in which B is the line broadening at half the maximum intensity, after subtracting the instrumental line broadening, in radians; K is a dimensionless shape factor, with a value close to unity; λ is the X-ray wavelength; θ is the Bragg angle. To further measure the elemental composition and chemical bonds at the surface of the samples, X-ray photoelectron spectroscopy (XPS) spectrum is collected. The XPS survey spectra and the three-element narrow scanning are presented in Fig. 1(g). In XPS survey, there are mainly three signals: C1s (at around 284.4 eV), O1s (at around 529.9–533.472 eV), and Au 4f (at around 83.9 eV). The Au signal is from the Au coated steel sample holder, which is used to limit the C and O contamination on the sample holder surface and serves as an internal energy calibration reference. There are some small peaks at around 320–360 eV, which are also from Au. Since Au is not the element of our interest and the intensity is quite low, they are not scanned. The resulting atomic concentration of the elements is summarized to be 96.32% C 1s and 3.68% O 1s. The XPS C 1s spectrum has 2 peaks centered at 284.4 and 291 eV respectively. The peak centered at 284.4 eV is assigned to C-C/C=C in aromatic rings, which is a characteristic of a sp^2 type C network. The higher binding energy shoulder peak at ~291 eV is due to π -π* satellite of the sp^2 type C. The O 1s spectrum shows three O environments. The low binding energy peak at ~529.9 eV is due to the iron oxide from signal of the steel sample

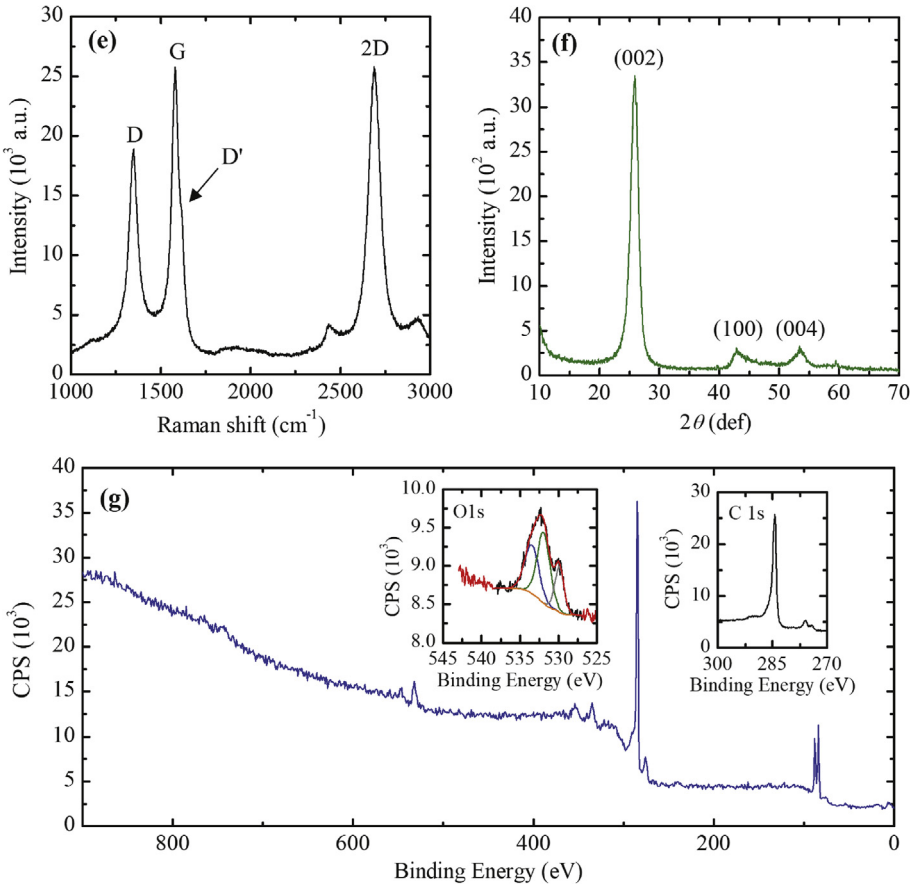

Fig. 1. (*continued*).

holder (only part of the steel sample holder is coated with Au). The peak at ~532.0 eV and the peak at ~533.5 eV are from C-O species and C=O species respectively in the CNT bundles. From these results, there are oxygen-containing functional groups on the surface of CNT bundles.

3. Thermal characterization and annealing method

3.1. Method for annealing

Three CNT bundles are annealed by applying large DC currents to them under high vacuum conditions. The three samples are denoted as S1, S2 and S3 respectively. Details of the three samples can be found in Table 1. Each sample is subjected to DC currents whose value is increased from low to high till the sample is burnt broken. The duration for each DC current are set to be 2 s for S1 and S2, and 20 s for S3. The voltage profiles over the samples during current annealing are collected using an oscilloscope. After each annealing, using the same experimental set-up, a TET measurement is conducted to measure the in-situ thermal diffusivity. It makes sure that the minimum and optimum current for improving thermal diffusivity can be observed clearly.

Table 1
The details of the measured CNT bundle samples.

Index	S1	S2	S3	S4
Suspended Length (mm)	2.37 ± 0.07	2.77 ± 0.04	2.37 ± 0.06	1.05 ± 0.04
Diameter (μm)	280 ± 12	222 ± 13	225 ± 10	44.4 ± 8

3.2. Method for measuring thermal diffusivity

The TET technique is a fast and robust method for measuring thermal diffusivity of various solid materials [38–42]. Fig. 2 shows details of experiment set-up and principle. Fig. 2 (a) shows a digital camera photo of the MWCNT bundles array, from which individual bundles are obtained. Fig. 2 (b) displays a microscopy image of a suspended CNT bundle sample. In the experiment, the CNT bundle is suspended between two gold coated silicon electrodes and connected using small amount of silver paste. Fig. 2 (c) shows the schematic of the experimental set-up. The sample is then put in a vacuum chamber, where the air pressure is maintained below 0.5 mTorr.

During TET measurement, a small step current (around 50 mA) is fed through sample by a current source to induce a fast joule heating. The voltage profiles are collected using an oscilloscope. Upon heating, the temperature of the sample has a fast increase and then reaches a steady state. The joule heat is transferred by thermal conduction along the length direction of the sample and thermal radiation to the environment. Heat convection can be neglected due to the low air pressure in the chamber. Thermal diffusivity is the thermal conductivity divided by density and specific heat capacity. During the TET measurement, two competing processes determine how fast/slow the temperature of the sample increases: one is the Joule heating, and the other is the heat conduction from the sample to the electrodes. A higher thermal diffusivity of the sample will lead to a faster temperature evolution and a shorter time to reach the steady state. Thus, the transient temperature change can be used to determine the thermal diffusivity. Assuming one dimensional heat transfer model, the normalized temperature

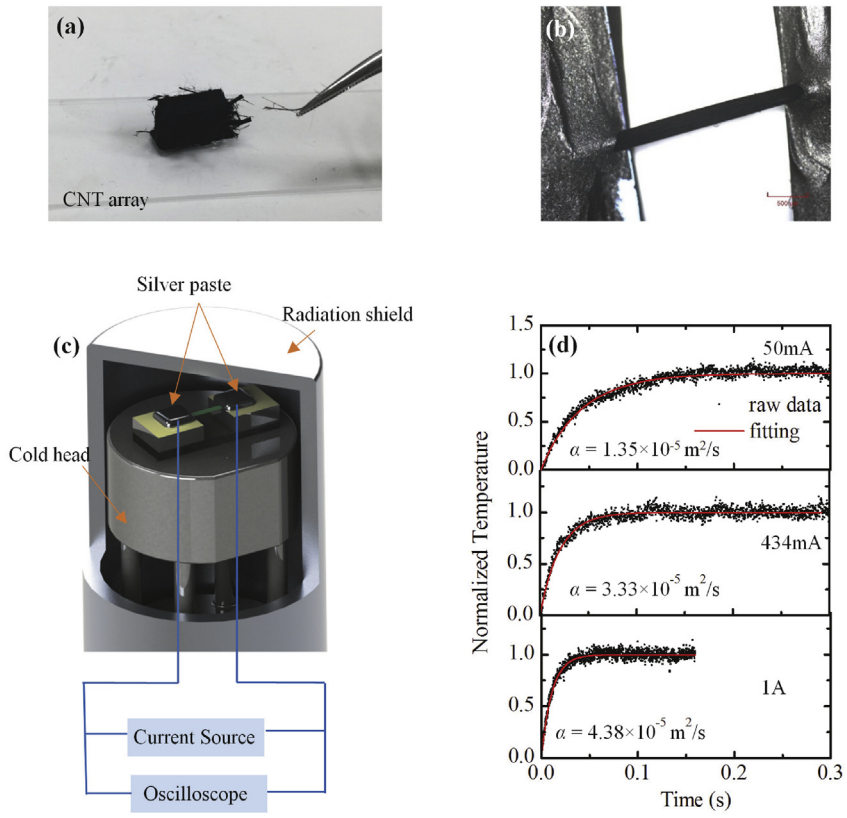

Fig. 2. Experimental set-up and principle of the transient electro-thermal (TET) technique for in-situ thermal characterization. (a) A digital camera photo of the MWCNT bundles array. (b) A microscopy image of a suspended CNT bundle sample. (c) A schematic of experimental set-up. (d) Selected normalized temperature profiles of TET of S1 after different currents annealing. The dots are raw data and lines are fitting curves from TET model. The corresponding thermal diffusivity values (α) are also presented in the figures. (A colour version of this figure can be viewed online.)

profile for this transient state can be derived as [38–42].

$$T^* \cong \frac{48}{\pi^4} \sum_{m=1}^{\infty} \frac{1-(-1)^m}{m^2} \frac{1-\exp\left[-m^2\pi^2\alpha_m t/L^2\right]}{m^2} \quad (1)$$

The current used for the TET measurement is around 50 mA. Within the small temperature range during joule heating in TET measurement, the temperature coefficient of resistance is reasonably assumed constant. Under this circumstance, the normalized temperature rise can be obtained by normalizing voltage profile. Since CNT bundles have a negative temperature coefficient of resistance, the voltage presents a decreasing and stabilizing pattern. Some of the normalized temperature profiles of TET of S1 after different currents annealing is presented in Fig. 2 (d), including data after 50 mA, 434 mA and 1 A annealing. As the annealing current is increased, the time for the voltage/temperature to reach steady state becomes shorter and shorter. This reveals that the thermal diffusivity of S1 is increased after CITA in Fig. 2 (d). From Fig. 2 (d), the thermal diffusivity after 434 mA annealing is higher than that after 1A, and the thermal diffusivity after 1A annealing is higher than that after 50 mA annealing. The corresponding effective thermal diffusivity is 1.35×10^{-5} m^2/s after 50 mA annealing, 3.33×10^{-5} m^2/s after 434 mA annealing, and 4.38×10^{-5} m^2/s after 1 A annealing. The thermal diffusivity evolution during the whole CITA process will be presented in section 4.2.

3.3. Method for measuring thermal conductivity

The steady-state electro-thermal (SET) technique [49,50] is used for measuring the thermal conductivity at low temperatures. The experimental set-up is the same as that of TET. The difference is that the SET technique utilizes the data before and at the steady state of the joule heating. During the measurement, a small DC current (around 50 mA) is applied to the sample to induce joule heating. In this method, κ at each temperature is obtained by:

$$\kappa = \frac{I^2 R_1 L(dR/dT)}{12 A_c \Delta R}. \quad (2)$$

In the equation, κ is the measured thermal conductivity, I the current flowing through the sample, R_1 the resistance of the sample at steady state, dR/dT is obtained by measuring the electrical resistance (R) at different temperature and differentiating the R-T curve, A_c the cross-sectional area of the sample, and ΔR the resistance change induced by the joule heating.

4. CITA results and discussion

4.1. The reduced electrical resistance

The electrical resistance of the samples is calculated using voltage data and DC current value ($R = V/I_{DC}$). Fig. 3 shows the resistance profiles of S3 during CITA of currents from 120 mA to 1.05 A. The evolutions consist of two stages. The first stage shows a sharp decreasing pattern, while the second stage presents a slowly decreasing behavior. The decrease in the first stage sources from fast joule heating like that in TET measurement. Within the first stage, the temperature of S3 is raised sharply by joule heating. The fast decreasing resistance reflects the fast temperature change.

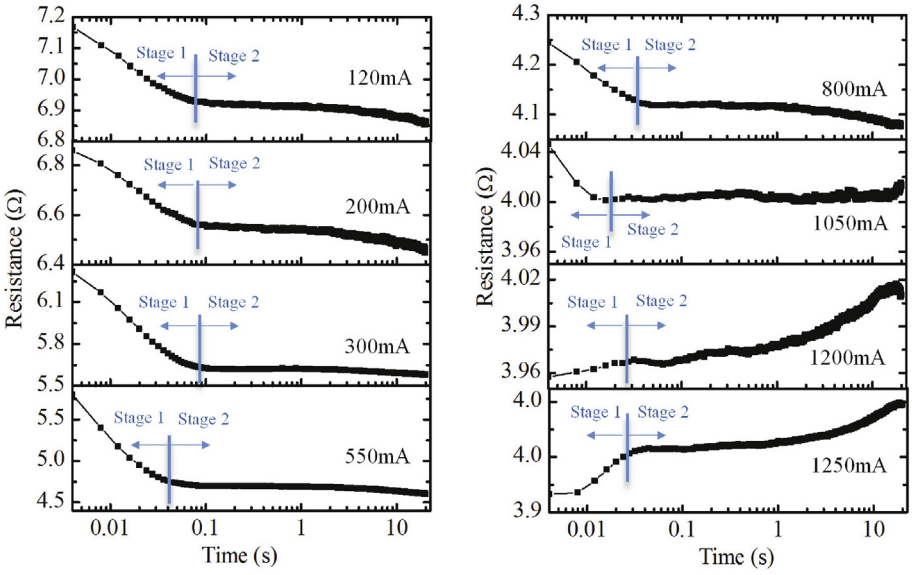

Fig. 3. The resistance profiles of S3 during the large current annealing from 120 mA to 1250 mA. Two-stage evolution is observed. (A colour version of this figure can be viewed online.)

After the first stage, the sample's temperature has reached steady or quasity-steady state. In the second stage, as the high density of electrical current continues to anneal the sample, the high temperature removes the contaminations absorbed on the surface of the CNT bundles and heals the lattice defects which impede the transport. More electron transport is facilitated. This results in a slowly decreasing resistance. Therefore, the resistance keeps decreasing slowly. Under the annealing current from 120 mA to 800 mA, the annealing effect is the dominant effect on changing electrical resistance in stage 2. Thus, the electrical resistance decreases slowly with time.

However, since the CNT bundles are composed of hundreds of thousands of individual CNTs aligned along the axial direction, the interface contact resistance among the neighboring CNTs is also another important factor affecting the overall electrical resistance of the samples. The thermal expansion coefficient is different among the CNTs with different level of defects. When temperature is raised by large joule heating, the thermal expansion mismatch results in a loosened connection among CNTs, which increases the interface contact resistance and the overall electrical resistance of the CNT bundle. When the annealing current is low, this effect is overshadowed by the annealing effect on the electrical resistance. When the annealing current exceeds 1050 mA, the thermal expansion mismatch becomes so significant that the effect of the increased electrical contact resistance starts to dominate the electrical resistance. Thus, under the annealing current from 1050 mA to 1250 mA, the overall electrical resistance starts to increase with time. It should be noted that this thermal expansion mismatch is a temporary effect. When the temperature of the sample cools down to room temperature, the connection among CNTs is recovered and the interface contact resistance goes down again. When measured at room temperature, the overall electrical resistance of CNT bundles after annealing is reduced compared to that before annealing. The resistance at room temperature will be discussed in the following section.

In addition to the joule heating effect and annealing effect, there is another effect which should be taken into consideration when analyzing the resistance change. When the distance between two adjacent CNTs is sufficiently small, electron tunneling takes place across the connecting sites under large current. This causes a nonlinear *I-V* curve of CNT bundles. Under small currents, the energy is not high enough for exciting electrons to overcome the energy barriers at the connection. Therefore, the original resistance measured at the beginning of *I-V* curve of CITA is much lower than that measured from small current. For example, the resistance profiles after 800–1250 mA show an original resistance of 3.9–4.25 Ω. However, the resistance measured by using a small current (46–50 mA) is much higher (>7 Ω). The resistance profiles measured using small current during TET will be discussed in the next paragraph [Fig. 4 (a)]. This discrepency indicates the existance of the electron tunneling. Thus, the slowly decreasing behavior of the electrical resistance profiles in the second stage is also a combination effect of permanent structural improvement from annealing and the nonlinear *I-V* curve under large current. This is an issue which requires further in-depth work.

The in-situ thermal and electrical characterization is conducted by alternating CITA process with TET measurement: a few minutes after each CITA (wait for the samples to cool down), TET measurement is conducted. The small current used for the TET measurement is in the range of 38–52 mA, which causes a ~1% resistance decrease in the samples. Fig. 4 shows the results for the resistance and thermal diffusivity. They are measured at room temperature after each annealing. The electrical resistance is measured by measuring the voltage and the current of the sample. The experimental uncertainty of the resistance is estimated to be about ±3%. For clarity, it is not presented in Fig. 4 (a). The resistance of the three samples [Fig. 4 (a)] begin to decrease when the heating current is increased to about 100 mA. For S1, it drops from the original value of about 7.4 Ω to the final value of about 6.8 Ω, which is 8% decrease. For S2 and S3, it decreases by 7.6% and 4.4% of their original resistance respectively. Overall, the electrical resistance is not improved significantly by CITA.

As illuminated before, the resistance decrease is mainly due to healing of structural defects and removing of impurities in CNT bundles. However, the resistance profiles do not follow a monotonically decreasing pattern. Instead, a valley is observed for all the three samples at around 200 mA. S3 presents an extra valley at around 800 mA. These valleys are attibuted to the removal of surface adsorbed content. Previous works reported that annealing reduced the adsorbed oxygen content on the surface of CNTs, which

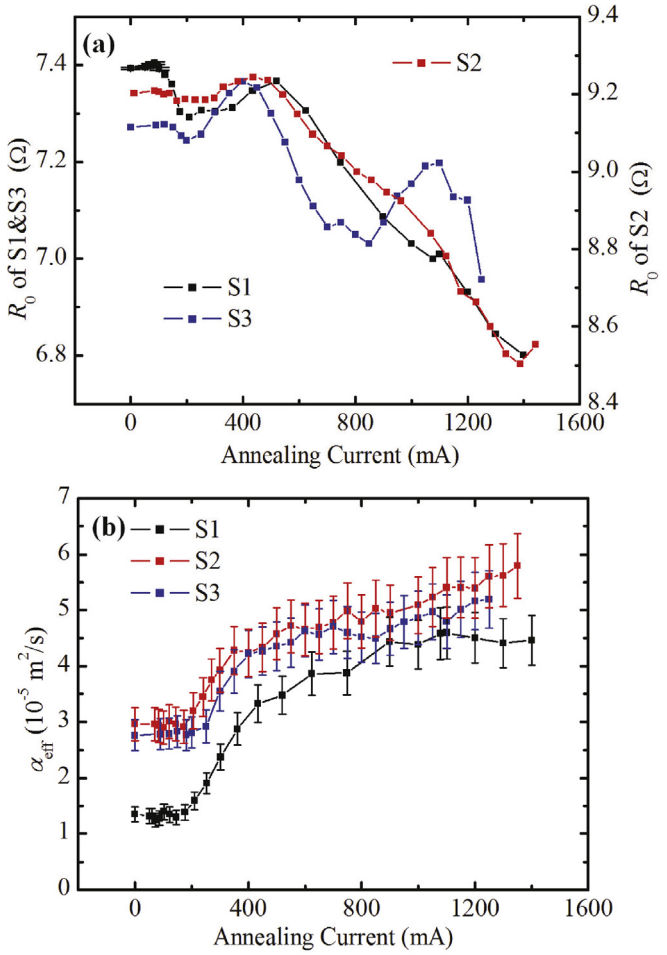

Fig. 4. The experimental result of CITA effect. (a) The electrical resistance against annealing current. The experimental uncertainty of the resistance is estimated to be about ±3%. For clarity, error bars are not presented in the figure. (b) Effective thermal diffusivity of CNT bundles against annealing current. (A colour version of this figure can be viewed online.)

could also weaken the tube-tube contacts such that carriers can now be trapped there [51]. Therefore, this should be the reason why a small increasing region of R_0 from 200 mA to 400–520 mA is observed. In CNT bundles, there are oxygen-containing C-O and C=O functional groups on the surface. The temperatures required for removing different oxygen groups are different, which causes an extra valley in resistance profile of S3.

4.2. The enhanced effective thermal diffusivity and phonon scattering principle

The effective thermal diffusivity (α_{eff}) after each annealing is summarized in Fig. 4(b) α_{eff} is increased significantly by CITA. The original α_{eff} of S2 and S3 is about 2.76-2.96 $\times 10^{-5}$ m^2/s. For S1, the original α_{eff} is lower (1.32×10^{-5} m^2/s). This indicates that S1 is originally inferior in quality than S2 and S3. Similar to the evolution of electrical resistance, low DC current (lower than 200 mA) has no effect on α_{eff}. α_{eff} stays constant before 200 mA. After being subjected to 200 mA CITA, α_{eff} of all the three samples begin to increase. For S2 and S3, α_{eff} keep increasing with the annealing current till burnt broken. Their α_{eff} before broken is about 5.80×10^{-5} and 5.20×10^{-5} m^2/s respectively, which accounts for 110% and 76% increase over the original thermal diffusivity. For S1, α_{eff} reaches a maximum and becomes relatively stable after being annealed by current higher than 897 mA. The stable value from 897 mA to 1.4 A indicates that the thermal diffusivity of the sample cannot be improved by CITA any further. This value represents a saturated thermal diffusivity of S1. The upper limit of α_{eff} of S1 is 4.44×10^{-5} m^2/s, which is 236% increase over the original value.

The threshold of electrical resistance and α_{eff} changed by current are different. The threshold of α_{eff} has a delay compared to that of R_0 at the beginning. Furthermore, no very obvious valleys are observed in the α_{eff} profiles. This indicates that α_{eff} is less sensitive to the small structure changes at inter-tube interfaces and inner alignment. As discussed above, removing oxygen contents at inter-tube interfaces impedes tunneling of electrons, which is responsible for the valleys in the resistance profiles. On the other hand, tunneling does not apply to phonons. Phonons are always scattered at inter-tube interfaces. Removing the oxygen contents only reduces the phonon scattering intensity, which facilitates propagation of phonons. Therefore, α_{eff} is monotonically enhanced by reduced impurities and inter-tube thermal contact resistance.

To further understand the thermal properties enhancement of our CNT bundles, temperature dependent thermal diffusivity and conductivity (κ) of a same CNT bundle sample from 295 K to 10 K are characterized. This sample is denoted as S4, whose details can be found in Table 1. Fig. 5 (a) shows the SEM image of S4. The annealing current is 20 mA. The temperature dependent α and thermal conductivity (κ) of S4 before and after CITA are presented and compared in Fig. 5 (b) and (c) respectively. The α- T curve is measured using the TET technique. The vacuum and stable low temperature environment is supplied by using the Janis closed cycle refrigerator (CCR) system. As temperature goes down, α first increases and then decreases. Before CITA, the peak of α- T curve is 6.30×10^{-5} m^2/s at 147.8 K. After annealing, the peak position shifts to 122.3 K at 8.82×10^{-5} m^2/s. α after CITA is higher than that before CITA. At RT, it has a 33.6% enhancement. At peak position, it has a 40% increase. This result demonstrates the thermal diffusivity of CNT bundle is improved consistently by CITA from RT to as low as 75 K. Below 75 K, α of after-annealing shows a decreasing behavior which is much faster than that before annealing.

The peak of the α-T curve is resulted from the special nanostructure of the CNT bundles. Phonons are the main heat carriers in carbon materials. For most of the carbon materials with seamlessly interconnected inner structures, phonon-phonon scattering (U-scattering) and phonon-defect scattering are the two main mechanisms controlling the thermal diffusivity. When temperature goes down, lattice vibration weakens and the phonon population decreases, which results in a reduced phonon scattering intensity and an increased phonon mean free path. Thus, their α monotonically increases as temperature goes down. In comparison, CNT bundles are composed of individual CNTs aligned along the axial direction. Besides the U-scattering and the impurities-phonon scattering [52,53], the tube-tube interface also makes a significant contribution to the phonon scattering [20,31]. Only phonons with a wave vector larger than $G/2$ (G is the reciprocal lattice vector of the first Brillouin zone) can participate in the thermal conduction by collision. At near RT, almost all phonons have enough energy to participate in the thermal conduction. Thus, phonon-phonon scattering dominates the thermal conduction. As temperature goes down, lattice vibration weakens and the phonon population reduces. The phonon-phonon scattering intensities decreases subsequently, which leads to an increase of α. Therefore, as temperature goes down from RT to 122.3 K- 147.8 K, α of S4 shows an increasing behavior.

As temperature goes down further, the phonon-phonon scattering becomes too weak to dominate thermal conduction. The effect of intra-tube defect scattering and tube-tube interface scattering becomes significant. The intra-tube defects induced

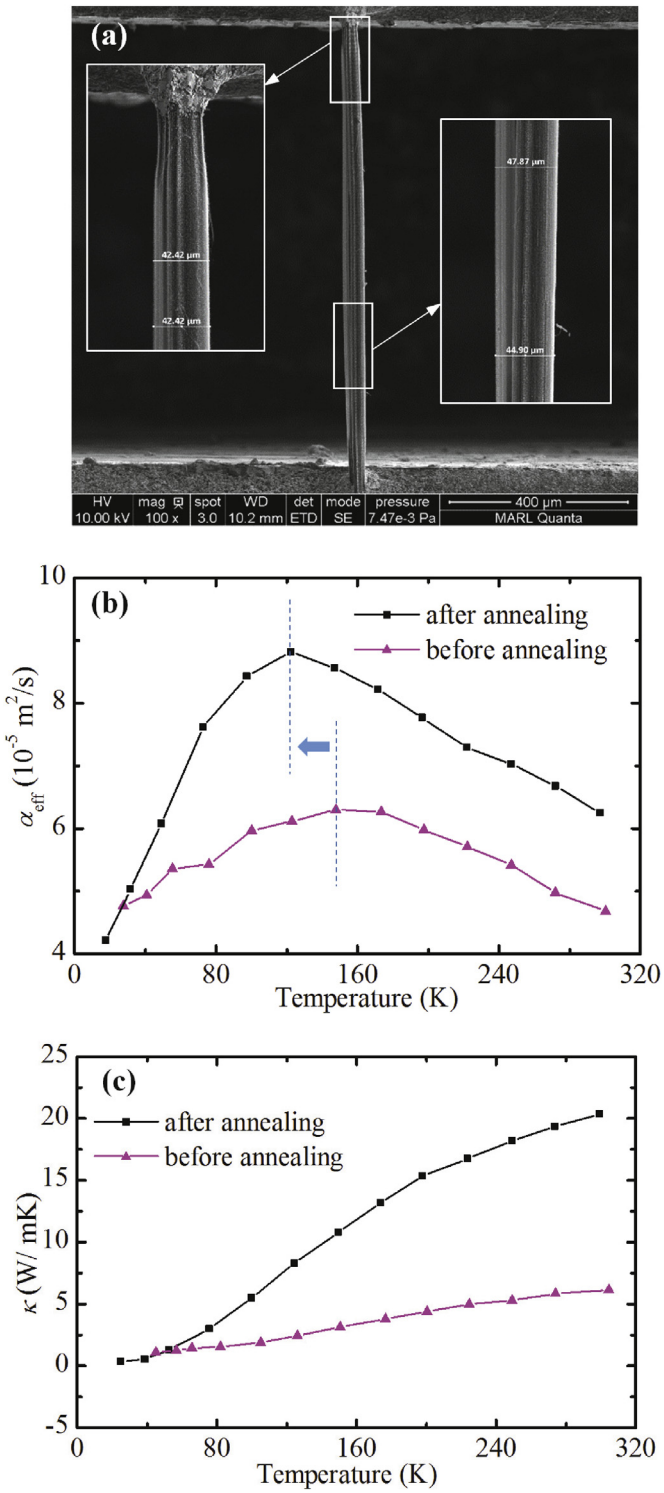

Fig. 5. (a) One of the SEM image of S4 after annealing. The insets are zoom-in images for diameter measurement. (b) The comparison of temperature-dependent thermal diffusivity of S4 before and after 20 mA CITA. (c) The comparison of temperature-dependent thermal conductivity of S4 before and after 20 mA CITA. (A colour version of this figure can be viewed online.)

phonon scattering intensity can be assumed independent of temperature. The tube-tube interface scattering starts to dominate the phonon scattering at low temperatures (below 122.3 K- 147.8 K). The decrease of α is resulted from the low-temperature induced structural change in the sample. From the structure characterization, the CNT bundle material is not a simple solid material. Instead, its inner structure is composed of hundreds of thousands of coil-like CNTs aligned along the axial direction. The thermal expansion coefficient is different for CNTs with different levels of defects. At low temperatures, the thermal expansion mismatch causes a deteriorated thermal contact among the neighboring CNTs, which provides more phonon scattering at the tube-tube interfaces. As a result, as temperature goes down to below 122.3 K- 147.8 K, the phonon scattering intensity increases with the decreased temperature. α starts to decreases. Therefore, the α- T profiles show a peak at around 122.3 K- 147.8 K.

During CITA, part of CNTs with higher density of structural defects and higher electrical resistance could be burnt or melt due to the localized higher joule heating power. This inner structure change results in a stronger ability in holding the inter-connection among neighboring CNTs. Therefore, after CITA, it requires lower temperature and higher thermal strain for deteriorating the interconnection. The temperature from which the decreasing behavior begins to emerge is lower after CITA. This stronger interconnection strength after CITA is the reason for the peak shift of the α- T curve. Before CITA, the peak of α-T curve is at 147.8 K. After annealing, the peak position shifts to 122.3 K. From the α- T curve, before CITA, the low temperature decreasing accounts for 24.3% over the peak value. After CITA, the decreasing takes 52.2% over the peak value. After CITA, the effect of low temperature on the interface scattering becomes more significant than that before CITA.

Fig. 5 (c) shows the temperature dependent thermal conductivity of S4 before and after CITA. The κ -T curve is measured using steady-state electro-thermal (SET) technique. The experiment set-up is the same as that of TET. Thus, the sample stays on the same experiment set-up during the whole thermal characterization and CITA process. Details of the SET technique can be found in the experiment section 3.3 and in our past work [49,50]. The measurement uncertainty for SET is estimated to be about ±10%. For clarity of comparison, the error bars are omitted in the figure. κ of after-annealing is consistently higher than that before-annealing. At RT, κ presents a 3.32-fold increase over the before-annealing value. This further proves that the structure of the sample has been significantly improved by CITA. Both κ profiles present a monotonically decreasing behavior as temperature goes down. This behavior is similar to that of defected graphite materials reported in previous works. Both κ tend to reach zero as the temperature approaches 0 K. The decreasing rate of κ is higher after annealing, which is resulted from the higher decreasing rate of α after annealing. The main reason for the different temperature-dependent behavior between the thermal diffusivity and thermal conductivity is the volumetric specific heat (ρc_p). ρc_p is also a function of temperature. At very low temperatures, ρc_p decreases with the decreased temperature very sharply. Since $\kappa = \rho c_p \times \alpha$, the fast decreasing ρc_p overshadows the peak of α-T. Thus, in the κ-T profile, the peak at around 122.3 K- 147.8 K in the α- T profile is not very visible.

4.3. The unevenly distributed annealing effect along length direction

Three samples S1-S3 are annealed using large electrical current till they are burnt broken. Fig. 6 (a)-(b) show the morphology of S1 after broken. From Fig. 6 (b), the hollow structure can be seen clearly. A clean and smooth breaking edge near the center point is observed. Instead of 45° breaking line (caused by tensile break), the breaking lines are almost perpendicular to the axial direction of the sample. This breaking morphology indicates that the breaking is mainly caused by melting under high temperature. For the three samples, the melting occurs under 1.4 A, 1.35 A and 1.25 A for S1, S2

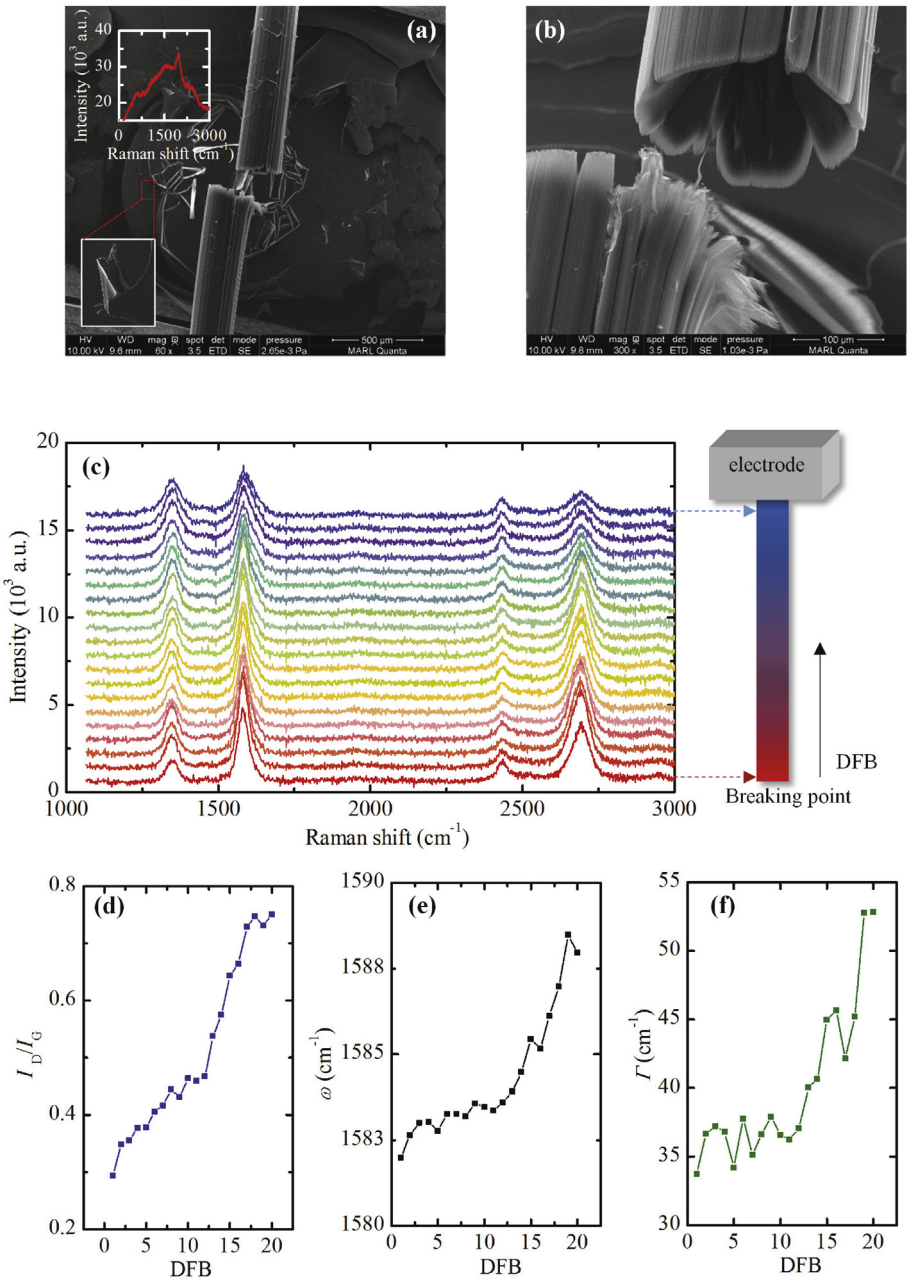

Fig. 6. The morphology and characterization of the structure after CITA. (a)–(b) The SEM images of the breaking point under low to high magnifications. The insets in figure (a) is the SEM and Raman signal of the amorphous carbon film sputtered on the glass substrate from the molten CNT bundle. (c) Change of the Raman signal with the distance from the breaking point (DFB). The Lorentz fitting result of the Raman signals, including (d) the ratio of intensity of the D peak to the G peak. (e) The Raman shift of G peak. (f) The full width at half maximum (FWHM) of G peak. (A colour version of this figure can be viewed online.)

and S3 respectively. The melting temperature will be evaluated and discussed in the next section. From Fig. 6 (a), the surface of glass substrate is also burnt by heat radiation from sample. The molten CNT bundle sputters a thin layer of carbon film on the surface of the glass substrate. A magnified SEM image of the thin layer of carbon film is displayed as an inset in Fig. 6 (a). Raman spectroscopy is conducted to find out the structure of the carbon film and is also displayed as an inset. The Raman spectrum is acquired under a 50× objective. It exhibits a very broad band centered at around 1558 cm^{-1}, which is a characteristic of amorphous carbon [54]. The peak at around 1960 cm^{-1} could be resulted from background reflection of the glass substrate and second-order combined scattering of the two main structures at 550 and 1550 cm^{-1} [55]. The melting of CNT bundles sputters a thin layer of amorphous carbon film on the glass substrate.

Under CITA heating, the temperature distribution along the axial direction of samples is not uniform: temperature near center point is much higher than that near electrodes. The higher temperature near center point results in a higher level of annealing. Therefore, annealing effect also varies along axial direction. To confirm this distribution, Raman spectroscopy data is acquired from different locations along the axial direction of S1 [Fig. 6 (c)]. Three pronounced peaks are observed. The G peak (around 1580 cm^{-1}) is from the stretching of the C-C bond in graphitic materials, which is usually assigned to zone center phonons of E_{2g} symmetry. The D peak at around 1350 cm^{-1} involves the resonantly enhanced

scattering of electrons via phonon emission by defects or sidewalls that breaks the basic symmetry of the graphene plane [47], which can be used as an indicator of structural disorder from amorphous carbon and other defects. The 2D peak (around 2690 cm^{-1}) is activated by double resonance processes [47], which indicates the long-range order. For sp^2 nanocarbons such as graphene and carbon nanotubes, Raman spectroscopy not only characterizes the density of doping, defects and other crystal disorder, but also provides information about crystallite size and the clustering of the sp^2 phase [48,56]. Although the Raman spectrum gives little information about how the CNTs assemble in the CNT bundles, it can tell about the structural disorder of the CNTs within CNT bundles. Since the CNT bundles consist of CNTs, when the structural disorder in CNTs is reduced, the structural quality of the CNT bundles is improved. Thus, the Raman spectra is used for characterizing the localized structural quality of the CNT bundles.

As the position of acquisition is moved from near electrode to the breaking point, the intensity of D peak shows an evident decrease, while the intensity of G and 2D peak both present a gradual increase. The intensity ratio of D band to G band (I_D/I_G) can be related linearly to the inverse of the crystallite size along the basal plane by the TK equation named after Tuinstra and Koenig [45,57]: $I_D/I_G = C(\lambda)/L_a$, in which $C(\lambda)$ is a constant related to the wavelength of the excitation laser (λ), and L_a is the cluster size. I_D/I_G can also be used for quantifying the density of disorder in CNTs. Analyzed using Lorenzian fitting, I_D/I_G is obtained and plotted against the distance from the breaking point (DFB) in Fig. 6 (d). I_D/I_G changes from 0.75 near electrode to 0.29 near breaking point, which accounts for 61.3% reduction. This variation points out a dramatically reduced degree of disorder and increased crystallite size near the breaking point. The Raman shift and full width at half maximum (Γ) of G peak are also presented in Fig. 6 (e) and (f). It shows that CITA results in a red-shifted G peak from 1588 cm^{-1} to 1582 cm^{-1}. Ring orders other than six tend to decrease the G peak height and increase its width. Γ of the G peak is a measure of the bond-angle disorder at sp^2 sites, and increases with the increased structure disorder [56]. Γ of G peak decreases from 53 cm^{-1} to 36.6 cm^{-1}, revealing increased graphitic structure order from two ends to the breaking point of the sample. The D' peak is quite weak, so it is omitted for the ease of fitting. The Raman results demonstrate the effect of CITA on reducing defect of CNTs along axial direction from near center point to the two ends.

4.4. Thermal conductivity evaluation by numerical calculation

4.4.1. The averaged and localized annealing effect

It should be noted that the experimentally measured α_{eff} in our TET experiment represents an averaged effect across the whole length of the samples. The annealing effect varies along axial direction as demonstrated in the previous section. In this section, to find out exactly how the localized thermal conductivity (κ) of CNTs changes with the localized temperature (T), finite difference modeling (FDM) is carried out to calculate the κ and T evolution along the axial direction during CITA and TET experiments. The FDM method has been widely used for solving temperature distribution and heat transfer problems [58,59]. To validate our FEM model for calculating the one-dimensional temperature distribution, we used this model to simulate a TET measurement process for a known material, Pt wire. The properties of Pt wire including thermal conductivity (71.6 W/m·K), specific heat (133 J/kg·K), density (21450 kg/m^3) [60], electrical resistivity ($0.1086 \times 10^{-6}\ \Omega$·m), and temperature coefficient of resistance (0.003927 K^{-1}) [61] are from references and used in the calculation. The length is set to be 5.08 mm, diameter is set to be 25.4 μm, and the DC current is set to be 78.06 mA, which is the same as that in an experimental study in our previous work [38]. The sample is divided into 1000 grids in the calculation. The evolution of the averaged temperature of the sample against time is calculated. Then we fit the simulated T-t curve and determine the thermal diffusivity. The resulting thermal diffusivity is $2.59 \times 10^{-5}\ m^2/s$ from our FDM method, which is very close to the value $2.51 \times 10^{-5}\ m^2/s$ at 300 K from literature [60]. The error is about 3.2%. It is conclusive that our FDM modeling can simulate the transient thermal behavior during TET with sufficient accuracy.

Due to the large length to diameter ratio of CNT bundles, only the axial direction heat transfer is considered. Besides, since the temperature distribution is symmetric around the center point along the axial direction, only half of the suspended sample needs to be calculated. The geometries of the half CNT bundle sample and the electrodes are depicted in Fig. 6 (c). The system has an initial temperature of 290 K. The length, diameter, and electrical resistance of the sample is set according to the experimental conditions. The volumetric specific heat of the CNT bundles at room temperature is calculated by $\rho c_p = \kappa/\alpha$, in which κ is measured using the SET technique, and α is the thermal diffusivity measured using TET technique. Details about the SET and TET techniques can be found in section 3.2 and 3.3. The resulting ρc_p before CITA is determined to be $2.1 \times 10^5\ J/m^3 \cdot K$. In the TET experiment, since the temperature increase is in a very small range, the variation of ρc_p within the small temperature range is negligible. In the CITA simulation, we are only interested in the steady-state temperature which is independent of ρc_p. Therefore, the ρc_p value is reasonably set to be a constant during simulation. Meshes are generated in the length direction with a grid size of 1 μm.

After CITA, κ improvement is different along the length direction. To simplify, we assume κ has a linear relationship with the distance from the center point (l_c). Near the center point of the sample, the temperature is the highest, so κ has the maximum value. It is denoted as κ_c. Since the two electrodes have much larger volume compared to sample, the temperature of the electrodes stays constant during the large current annealing. The two ends of sample near electrodes experiences only very small temperature increase, so κ of two ends of the sample in the electrodes is assumed unchanged. It is denoted as κ_0. Therefore, the thermal conductivity is expressed as $\kappa = \kappa_0 + (\kappa_c - \kappa_0) \times (L - l_c)/L$, in which L is the suspended length of the sample. Here, κ_0 is the thermal conductivity of sample before annealing. It is measured using SET technique which is presented in section 3.3 [49,50].

There are two steps in the simulation. In the first step, the TET measurement process at RT is simulated. The objective is to find κ_c. Different κ_c values are tried to calculate the evolution of the averaged sample temperature (T_a) during TET heating. The temperature profile which gives the best fitting of the experimental data is selected. The corresponding κ_c value is determined as the thermal conductivity value at the center point. The second step is to simulate the CITA process using the obtained thermal conductivity profile. The purpose is to find the localized temperature distribution over space during CITA. At time equals zero, a large current is supplied through the length direction of the sample to induce joule heating. The temperature evolution during the joule heating process is calculated. Since the experiment is conducted in a vacuum environment, heat convection effect is neglected. Only heat conduction, heat radiation with environment, and joule heating is taken into consideration during this process.

In TET measurement, since the temperature increase is quite small ($\Delta T \ll T$) and the sample's aspect ratio is very large, the radiation effect contributes insignificantly for determining thermal diffusivity (less than 1.5%). Under this situation, error from emissivity is very small in TET measurement at RT. During CITA, because of the very high temperature induced by joule heating, heat

radiation effect becomes one of the most important factors in thermal transport. From literature, the emissivity of SWNTs forest is reported to be 0.98–0.99 across a wide spectral range from UV (200 nm) to far infrared (200 μm) [62]. In our simulation, the CNT bundle is treated as a black body (emissivity = 1). This will result in a overestimated radiation effect, which gives an underestimated temperature increase of the sample. However, if we reduce the emissivity by 10%, the temperature increase will rise by ~2.4% according to our calculation. Thus, error from emissivity uncertainty is still very small.

Fig. 7 shows the simulation result, in which figure (a) shows the effective thermal diffusivity (α_{eff}) of the sample as a function of the averaged sample temperature (T_a). α_{eff} is improved at a very high rate in the temperature range of 546–1093 K for S1, 620–941 K for S2, and 637–783 K for S3. After the fast increasing temperature zone, increase of α_{eff} slows down and finally becomes relatively stable. α_{eff} is an averaged value representing the thermal properties of the whole length of samples. To investigate how the localized thermal conductivity is increased by the localized high temperature, the center point of sample is studied in detail. The right *y* axis in Fig. 7 (b) presents the thermal conductivity of the center point (κ_c) as a function of the annealing temperature at the center point (ΔT_c). κ_c shows a similar behavior as the effective thermal diffusivity. For S1, κ_c has a fast increase between 303 K and 1497 K and then becomes relatively stable till breaking at 2202 K. For S2 and S3, before breaking, κ_c has a fast increase temperature zone and then a slow increase temperature zone. The changing points of the increasing rate are 888 K and 671 K for S2 and S3 respectively. The highest κ_c of the three samples are 41.3 W/m·K at 2491.8 K for S1, 32.6 W/m·K at 2995.7 K for S2, and 28.3 W/m·K at 2537.0 K for S3 respectively.

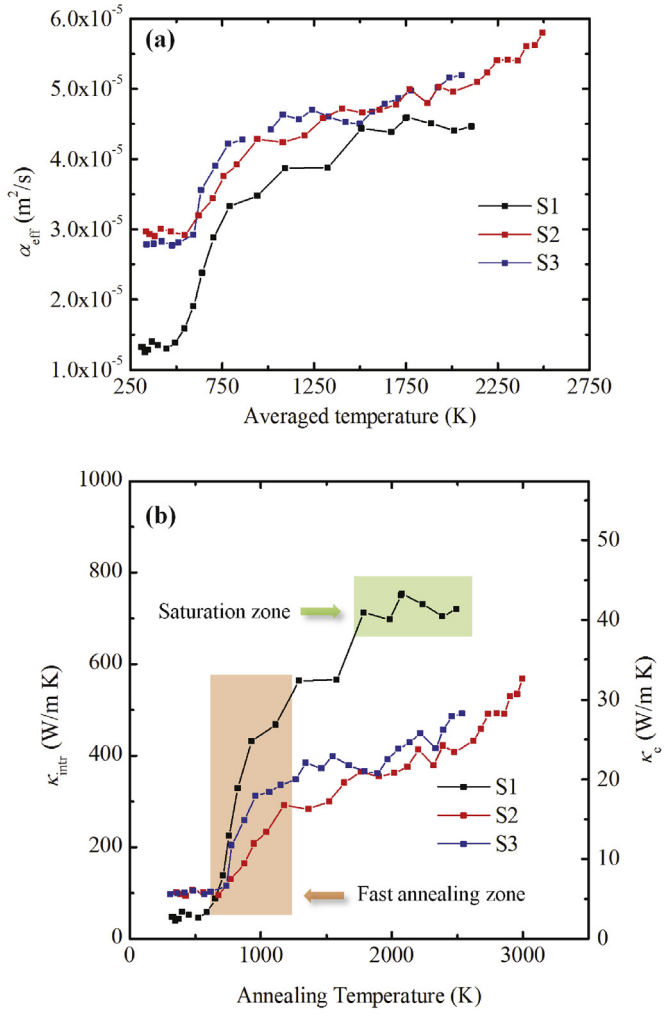

Fig. 7. (a) The effective thermal diffusivity of CNT bundles against the averaged sample temperature during CITA. It shows an averaged effect of annealing. (b) Right *y* axis: the thermal conductivity of the center point of CNT bundles against the temperature of the center point during CITA. It shows the localized annealing effect at the center point. Left *y* axis: calculated intrinsic thermal conductivity of CNT walls (κ_{intr}) against the annealing temperature. The orange rectangular shows the fast annealing zone. The green rectangular indicates a saturated annealing state of S1. (A colour version of this figure can be viewed online.)

4.4.2. The intrinsic α and κ of CNT walls in CNT bundles after annealing

To realize the desired performance of CNT bundles in novel applications requires sophisticated understanding and control of thermal transport at the nanoscale. The thermal conductivity of the CNT bundles is significantly influenced by two factors. One factor is the assembling pattern of the bundles, and the other factor is the intrinsic κ of CNT walls (κ_{intr}) within the bundles. CNT bundles consist of CNTs with walls formed by multiple rolled layers of atom-thick sheet of carbon. From XRD result [Fig. 1 (f)], the interlayer spacing between layers in CNT walls (3.4 Å) is very close to that in graphite. κ_{intr} means the ability of the CNT walls to conduct heat along the axial direction. The thermal transport in CNT bundles occurs via phonon propagation along the CNTs walls. It is of great interest to study the thermal conductivity of the CNT walls as it plays a big role in determining the overall thermal conductivity of CNT bundles. In this section, we further study the evolution of κ_{intr} against the annealing temperature. This will lay the foundation for a better understanding of the thermal conductivity of CNT bundles, as well as provide theoretical guidance for further improvement of thermal conductivity of CNT bundles in the future.

The models for computing the thermal conductivity of two-phase materials based on the thermal conductivity of the two phases and their volume fraction have been systematically compared in our previous work [63]. However, these models are not applicable for calculating the intrinsic solid thermal conductivity within the unique structure of CNT bundles. For example, the Maxwell effective medium approach has been used for calculating the solid conduction in uniformly distributed solid-gas systems [64], but it is not applicable for the CNT bundles of highly aligned fine structures with very high aspect ratio. In general, the Maxwell model is expected to be valid at low volume fractions ($\varphi \ll 1$, in the order of 0). Also it is assumed that the domains are spatially separated and the interactions among inclusions do not matter [65]. However, the volume fraction of CNT bundles is not very low ($\varphi \sim 13\%$) and the CNTs are connected with each other. In addition, the CNT bundles have highly ordered structure inside. As seen from the SEM images, the CNTs in the sample have a hollow cylinder structure. The cylinder walls are composed of coil-like structured CNTs with a specific curvature. Also the CNTs are aligned along the axial direction. Thus, the solid network within CNT bundles is not like randomly distributed particles as that described in the Maxwell model [63]. The Maxwell approach is not applicable for CNT bundles.

The measured volumetric specific heat of CNT bundles [$(\rho c_p)_{CNT\ bundles}$] in our work is about 2.1×10^5 J/m^3 K at RT. For full dense carbon materials, such as graphite, the volumetric specific heat is generally about 1.6×10^6 J/m^3 K [66]. The discrepancy between CNT bundle and other full dense carbon materials is due to the large viodage in the sample. As seen from the SEM images in Fig. 1, the CNT bundles are hollow cylinders, where large opening space is observed inside the cylinder walls. The cylinder wall is composed of individual CNTs, which leaves voids between the neighboring CNTs.

All of the viods contribute to the much lower density of CNT bundles than that of full dense carbon materials.

In this work, we calculate the intrinsic thermal conductivity from the heat transfer path aspect by calculating the intrinsic thermal diffusivity of CNT walls (α_{intr}) and the volumetric specific heat of CNT walls separately. The method for calculating α_{intr} is based on the following model. One-dimensional heat transfer model is assumed in CNTs, where the heat conduction in the radial direction is neglected. This is a reasonable assumption and has been widely used in literature [15]. For one-dimensional heat transfer model without considering heat radiation, the normalized temperature profile during TET measurement is derived as that in equation (1). From equation (1), it can be seen clearly that the thermal diffusivity is proportional to the square of the length of the sample. For CNT bundles, this length is the suspended sample length. For CNTs, because heat is conducted along the path of the curved CNTs, the intrinsic thermal diffusivity of CNTs should be larger than the measured effective thermal diffusivity of CNT bundles. Take an extreme case for example, for one single curved CNT, when measured using the TET technique, the length used in equation (1) should be the total length of the 3D curve, not the straight distance between the two electrodes. This method has been used in our previous work for characterizing a single carbon nanocoil. The length for calculating the real thermal diffusivity was the total length of the carbon nanocoil by taking the helical morphology into consideration [67]. In our work, we used the straight-line length of the CNT bundle sample for calculating α_m of CNT bundles. To further obtain the intrinsic thermal diffusivity of the CNTs in the bundles, the curved morphology should be taken into consideration. From the above analysis, $\alpha_m/L^2 = \alpha_{intr}/L_{curve}^2$, in which L is the straight-line length, L_{curve} is the total length of the curved CNT. As is indicated in the SEM image in Fig. 1 (b), CNTs in the samples resemble a coil-like shape. The red line shows part of the shape of one single CNT. During joule heating, heat is transferred following the path of the curve from point A to B. The length of the curve is much larger than the straight-line distance between A and B. After evaluating several heat transfer pathes, the average ratios of the actual heat transfer route over the axial-direction distance in the sample is estimated to be 1.24. The 3D length of the CNTs is larger than that observed in the 2D picture. Taking the radial symmetry property of the CNT bundle into consideration, since $\sqrt{L_x^2 + L_y^2} = 1.24$, the 3D ratio of the curvatural length of CNTs over the straight line length can be estimated as $\sqrt{L_x^2 + L_y^2 + L_z^2} = 1.52$. Thus, the intrinsic thermal diffusivity of the CNTs at the center point of the bundle can be calculated as $\alpha_{intr} = 1.52^2 \times \alpha_c$. α_c is the thermal diffusivity of the center point of the bundle. It can be calculated by $\alpha_c = \kappa_c/(\rho c_p)$. The intrinsic thermal diffusivity of CNT walls is equal to the intrinsic thermal diffusivity of CNTs since the heat is conducted along the wall of CNTs. This value includes the effect of phonon scattering within CNT walls and at the interfaces among the neighboring CNTs.

To obtain κ_{intr}, the volumetric specific heat of the CNT walls is needed. The effect of the hollow structure of CNTs and other void space in the CNT bundles needs to be taken out. It is known that MWNTs consist of multiple rolled layers (concentric tubes) of graphene. The interlayer distance in MWNTs is close to the distance between graphene layers in graphite, approximately 3.4 Å. Thus, the density ($\rho_{graphite}$) and specific heat of graphite ($c_{pgraphite}$) is used for calculating the volumetric specific heat of CNT walls. Using the density of graphite (2230 kg/m^3) and specific heat value of graphite (710 J/Kg·K at RT) [66], κ_{intr} can be evaluated as $\kappa_{intr} = \alpha_{intr} \times \rho_{graphite} \times c_{pgraphite}$. The result against annealing temperature is plotted in Fig. 7 (b) (left y axis).

κ_{intr} presents a three-stage process as the annealing temperature increases from RT to as high as the melting temperature of CNTs. κ_{intr} of S1 has a fast increasing rate from about 593 K to 928 K. After 928 K annealing, the increasing rate of κ_{intr} is reduced. κ_{intr} finally reaches a saturation value after 1787 K. Increasing annealing current does not improve κ_{intr} any more. For S2 and S3, κ_{intr} first increases quickly and then keeps increasing slowly till broken. There is a changing point of increasing rate, which is 1178 K and 961 K for S2 and S3 respectively. Before annealing, κ_{intr} is about 39.3 W/m·K for S1, and 98.7 W/m·K for S2 and S3. After annealing, κ_{intr} goes to 753.7 W/m·K, 568.1 W/m·K and 492.1 W/m·K for S1, S2 and S3 respectively. The results indicate that the CITA dramatically increases κ_{intr}, which is brought up to 5–19 times higher than that before annealing. However, κ_{intr} after annealing is still not as high as the reported highest value of highly oriented pyrolytic graphite (~2000 W/m·K at RT). The reason is the residual impurities as well as the inter-tube thermal contact resistance, which cannot be removed by CITA. Based on our result, the most efficient temperature range for improving κ_{intr} is in the range of 600–1100 K. Within that temperature range, κ_{intr} is enhanced dramatically. This provides details for the sequential thermal conductivity enhancement process by CITA.

CITA has a higher effect on the thermal conductivity of S1 than the other two samples. The reason can be interpreted as following. The vertically aligned CNT bundles arrays are synthesized by CVD method on a Si wafer, and the single CNT bundles with diameter of about 200 μm are collected by peeling them off from the MWCNT bundles array. Although the dimensions of S1 are similar to S2 and S3, the quality is quite different. Before annealing, α_{eff} of S1 is two-times lower than the other two samples, which demonstrates that the quality of S1 is inferior than S2 and S3 (S1 could have more functional groups). The higher defects and impurities density endows S1 more room to improve. Another reason is the early breaking of S2 and S3. As seen from Fig. 7 (b), the two samples are burnt broken before their thermal conductivity reach a saturation value. Before broken, κ_{intr} still presents an increasing behavior. The early breaking is a consequence of localized overheating due to localized structure defects. In comparison, the thermal conductivity of S1 reaches its saturated value before broken. The melting temperature of the three samples are 2491 K, 2996 K, and 2537 K respectively. Literature reported a very high melting temperature of perfect single-walled CNT to be around 4800 K. However, the existence of defects caused a premelting temperature at around 2600 K [68]. The melting temperature of the three samples are consistent with the literature value. The difference could be resulted from the different defect density in the sample and the thermal strain effect.

The thermal conductivity improvement result is very promising compared to the previously reported thermal annealing or combined annealing results. Jin et al. reported a 9-time increase in the thermal conductivity at RT for MWCNT bundles after the sample was annealed at 2800 °C in Ar for 4 h [31]. Matsumoto et al. conducted a combined annealing. After optimum (at 800 °C, 150 A cm^{-2} for 1 min) treatment to single-walled CNTS, the resulting electrical and thermal properties presented a 3.1–3.7 times increase [36]. Our results from sole current-induced thermal annealing give a 5–19 times thermal conductivity increase. This result demonstrates the high efficiency of the CITA in improving thermal conductivity of MWCNTs. In addition, applying current can also help prevent undesirable structure changes during direct thermal annealing. Matsumoto et al. attributed the increased thermal and electrical properties of single-walled CNTs during high temperature annealing to the increased wall number, diameter, and crystallinity. The change in wall number and diameter could be undesirable, which can be prevented by applying current to the sample while being thermally treated simultaneously [53]. Therefore, CITA is demonstrated to be a very effective method for

purifying CNTs materials.

5. Conclusion

In this work, the sequential process of current-induced thermal annealing on improving the structure and thermal conductivity of CVD grown CNT bundles was studied for the first time. By combining current annealing in vacuum environment and in-situ TET characterization, the statistical errors from sample-wide structure variation and contamination during sample transfer/preparation process can be averted. The electrical resistance reduction and thermal diffusivity improvement of the same samples at different current levels were reported. The annealing resulted in a 4.4%–8% reduction in the electrical resistance, and 76%–236% increase in the effective thermal diffusivity. The thermal diffusivity and thermal conductivity of a same sample from RT down to 10 K before and after CITA are measured and compared to better understand the annealing effect. CITA process reduced defects within CNTs, and strengthened the inter-tube connections, which reduced the phonon scattering intensity considerably. This explains the much higher thermal conductivity after CITA. Raman spectroscopy was used to characterize the sp^2 bonding carbon structure improvement along the length direction of the bundles, which gives a 61.3% decrease in I_D/I_G at near breaking point compared to near electrodes. The thermal properties against annealing current were translated into a temperature dependent profile by finite difference modeling. CITA resulted in a 5–19 times thermal conductivity increase from about 2.3 W/m·K to 43.1 W/m·K at the most annealed region of CNT bundles. By taking the curvature and void space effect into consideration, the intrinsic thermal conductivity of CNT walls in the bundle was also evaluated. It increased from about tens of W/m·K to as high as 753.7 W/m·K at RT. Based on our result, the most efficient temperature range for improving κ_{intr} is in the range of 600–1100 K. This work sheds light on the understanding of thermal properties evolution during current induced thermal annealing process.

Acknowledgements

Support of this work by National Science Foundation (CBET1235852, CMMI1264399), Department of Energy (DENE0000671, DE-EE0007686), Iowa Energy Center (MG-16-025, OG-17-005) and Chinese National Science Foundation for Young Scientists (51602011) is gratefully acknowledged. The contribution to this work by G.E. was supported by the U.S. Department of Energy, Office of Science, Basic Energy Sciences, Materials Sciences and Engineering Division.

References

[1] S. Park, M. Vosguerichian, Z.A. Bao, A review of fabrication and applications of carbon nanotube film-based flexible electronics, Nanoscale 5 (5) (2013) 1727–1752.
[2] S.N. Habisreutinger, T. Leijtens, G.E. Eperon, S.D. Stranks, R.J. Nicholas, H.J. Snaith, Carbon nanotube/polymer composites as a highly stable hole collection layer in perovskite solar cells, Nano Lett. 14 (10) (2014) 5561–5568.
[3] H. Sun, X. You, J.E. Deng, X.L. Chen, Z.B. Yang, J. Ren, H.S. Peng, Novel graphene/carbon nanotube composite fibers for efficient wire-shaped miniature energy devices, Adv. Mater. 26 (18) (2014) 2868–2873.
[4] Z. Li, S.A. Kulkarni, P.P. Boix, E.Z. Shi, A.Y. Cao, K.W. Fu, S.K. Batabyal, J. Zhang, Q.H. Xiong, L.H. Wong, N. Mathews, S.G. Mhaisalkar, Laminated carbon nanotube networks for metal electrode-free efficient perovskite solar cells, ACS Nano 8 (7) (2014) 6797–6804.
[5] R.H. Baughman, A.A. Zakhidov, W.A. de Heer, Carbon nanotubes - the route toward applications, Science 297 (5582) (2002) 787–792.
[6] M. Hakamada, A. Moriguchi, M. Mabuchi, Fabrication of carbon nanotube/NiOx(OH)(y) nanocomposite by pulsed electrodeposition for supercapacitor applications, J Power Sources 245 (2014) 324–330.
[7] K. Saetia, J.M. Schnorr, M.M. Mannarino, S.Y. Kim, G.C. Rutledge, T.M. Swager, P.T. Hammond, Spray-Layer-by-Layer carbon nanotube/electrospun fiber electrodes for flexible chemiresistive sensor applications, Adv. Funct. Mater. 24 (4) (2014) 492–502.
[8] M.M.J. Treacy, T.W. Ebbesen, J.M. Gibson, Exceptionally high Young's modulus observed for individual carbon nanotubes, Nature 381 (6584) (1996) 678–680.
[9] M.F. Yu, O. Lourie, M.J. Dyer, K. Moloni, T.F. Kelly, R.S. Ruoff, Strength and breaking mechanism of multiwalled carbon nanotubes under tensile load, Science 287 (5453) (2000) 637–640.
[10] B.G. Demczyk, Y.M. Wang, J. Cumings, M. Hetman, W. Han, A. Zettl, R.O. Ritchie, Direct mechanical measurement of the tensile strength and elastic modulus of multiwalled carbon nanotubes, Mater. Sci. Eng., A 334 (1–2) (2002) 173–178.
[11] Z.C. Wu, Z.H. Chen, X. Du, J.M. Logan, J. Sippel, M. Nikolou, K. Kamaras, J.R. Reynolds, D.B. Tanner, A.F. Hebard, A.G. Rinzler, Transparent, conductive carbon nanotube films, Science 305 (5688) (2004) 1273–1276.
[12] J. Zaumseil, Single-walled carbon nanotube networks for flexible and printed electronics, Semicond. Sci. Technol. 30 (7) (2015) 074001.
[13] Z. Han, A. Fina, Thermal conductivity of carbon nanotubes and their polymer nanocomposites: a review, Prog. Polym. Sci. 36 (7) (2011) 914–944.
[14] E. Pop, D. Mann, Q. Wang, K. Goodson, H. Dai, Thermal conductance of an individual single-wall carbon nanotube above room temperature, Nano Lett. 6 (1) (2006) 96–100.
[15] M. Fujii, X. Zhang, H. Xie, H. Ago, K. Takahashi, T. Ikuta, H. Abe, T. Shimizu, Measuring the thermal conductivity of a single carbon nanotube, Phys. Rev. Lett. 95 (6) (2005) 065502.
[16] C.H. Yu, L. Shi, Z. Yao, D.Y. Li, A. Majumdar, Thermal conductance and thermopower of an individual single-wall carbon nanotube, Nano Lett. 5 (9) (2005) 1842–1846.
[17] P. Kim, L. Shi, A. Majumdar, P. Mceuen, Thermal transport measurements of individual multiwalled nanotubes, Phys. Rev. Lett. 87 (21) (2001) 215502.
[18] M. Bauer, Q. Pham, C. Saltonstall, P. Norris, Thermal conductivity of vertically aligned carbon nanotube arrays: growth conditions and tube inhomogeneity, Appl. Phys. Lett. 105 (15) (2014), 2608–1243.
[19] W. Yi, L. Lu, D.L. Zhang, Z.W. Pan, S.S. Xie, Linear specific heat of carbon nanotubes, Phys. Rev. B 59 (14) (1999) R9015–R9018.
[20] X.P. Huang, J.M. Wang, G. Eres, X.W. Wang, Thermophysical properties of multi-wall carbon nanotube bundles at elevated temperatures up to 830 K, Carbon 49 (5) (2011) 1680–1691.
[21] D.J. Yang, Q. Zhang, G. Chen, S.F. Yoon, J. Ahn, S.G. Wang, Q. Zhou, Q. Wang, J.Q. Li, Thermal conductivity of multiwalled carbon nanotubes, Phys. Rev. B 66 (16) (2002) 165440.
[22] J. Hone, M. Whitney, C. Piskoti, A. Zettl, Thermal conductivity of single-walled carbon nanotubes, Synth. Met. 103 (4) (1999) 2514–2516.
[23] M.J. Bronikowski, CVD growth of carbon nanotube bundle arrays, Carbon 44 (13) (2006) 2822–2832.
[24] N. Srivastava, H. Li, F. Kreupl, K. Banerjee, On the applicability of single-walled carbon nanotubes as VLSI interconnects, IEEE T Nanotechnol. 8 (4) (2009) 542–559.
[25] W. Huang, Y. Wang, G.H. Luo, F. Wei, 99.9% purity multi-walled carbon nanotubes by vacuum high-temperature annealing, Carbon 41 (13) (2003) 2585–2590.
[26] R. Andrews, D. Jacques, D. Qian, E.C. Dickey, Purification and structural annealing of multiwalled carbon nanotubes at graphitization temperatures, Carbon 39 (11) (2001) 1681–1687.
[27] S. Musso, M. Giorcelli, M. Pavese, S. Bianco, M. Rovere, A. Tagliaferro, Improving macroscopic physical and mechanical properties of thick layers of aligned multiwall carbon nanotubes by annealing treatment, Diam. Relat. Mater. 17 (4–5) (2008) 542–547.
[28] J. Chen, J.Y. Shan, T. Tsukada, F. Munekane, A. Kuno, M. Matsuo, T. Hayashi, Y.A. Kim, M. Endo, The structural evolution of thin multi-walled carbon nanotubes during isothermal annealing, Carbon 45 (2) (2007) 274–280.
[29] P.H. Maheshwari, R. Singh, R.B. Mathur, Effect of heat treatment on the structure and stability of multiwalled carbon nanotubes produced by catalytic chemical vapor deposition technique, Mater. Chem. Phys. 134 (1) (2012) 412–416.
[30] Y.A. Kim, H. Muramatsu, T. Hayashi, M. Endo, M. Terrones, M.S. Dresselhaus, Thermal stability and structural changes of double-walled carbon nanotubes by heat treatment, Chem. Phys. Lett. 398 (1–3) (2004) 87–92.
[31] R. Jin, Z.X. Zhou, D. Mandrus, I.N. Ivanov, G. Eres, J.Y. Howe, A.A. Puretzky, D.B. Geohegan, The effect of annealing on the electrical and thermal transport properties of macroscopic bundles of long multi-wall carbon nanotubes, Physica B 388 (1–2) (2007) 326–330.
[32] J. Moser, A. Barreiro, A. Bachtold, Current-induced cleaning of graphene, Appl. Phys. Lett. 91 (16) (2007) 183.
[33] B.Q. Wei, R. Vajtai, P.M. Ajayan, Reliability and current carrying capacity of carbon nanotubes, Appl. Phys. Lett. 79 (8) (2001) 1172–1174.
[34] P.J.F. Harris, Structural transformation of natural graphite by passage of an electric current, Carbon 107 (2016) 132–137.
[35] K. Bolotin, K. Sikes, J. Hone, H. Stormer, P. Kim, Temperature-dependent transport in suspended graphene, Phys. Rev. Lett. 101 (9) (2008) 096802.
[36] N. Matsumoto, A. Oshima, M. Yumura, D.N. Futaba, K. Hata, Current treatment of bulk single walled carbon nanotubes to heal defects without structural change for increased electrical and thermal conductivities, Nanoscale 7 (19) (2015) 8707–8714.

[37] K.I. Bolotin, K.J. Sikes, Z. Jiang, M. Klima, G. Fudenberg, J. Hone, P. Kim, H.L. Stormer, Ultrahigh electron mobility in suspended graphene, Solid State Commun. 146 (9–10) (2008) 351–355.
[38] J. Guo, X. Wang, Thermal characterization of microscale conductive and nonconductive wires using transient electrothermal technique, J. Appl. Phys. 101 (2007) 063537.
[39] H. Lin, S. Xu, Y.Q. Zhang, X.W. Wang, Electron transport and bulk-like behavior Of Wiedemann-franz law for sub-7 nm-thin iridium films on silkworm silk, ACS Appl. Mater. Interfaces 6 (14) (2014) 11341–11347.
[40] J. Liu, T.Y. Wang, S. Xu, P.Y. Yuan, X. Xu, X.W. Wang, Thermal conductivity of giant mono- to few-layered CVD graphene supported on an organic substrate, Nanoscale 8 (19) (2016) 10298–10309.
[41] Z. Cheng, M. Han, P.Y. Yuan, S. Xu, B.A. Cola, X.W. Wang, Strongly anisotropic thermal and electrical conductivities of a self-assembled silver nanowire network, RSC Adv. 6 (93) (2016) 90674–90681.
[42] Z.L. Xu, X.W. Wang, H.Q. Xie, Promoted electron transport and sustained phonon transport by DNA down to 10 K, Polymer 55 (24) (2014) 6373–6380.
[43] G. Eres, A.A. Puretzky, D.B. Geohegan, H. Cui, In situ control of the catalyst efficiency in chemical vapor deposition of vertically aligned carbon nanotubes on predeposited metal catalyst films, Appl. Phys. Lett. 84 (10) (2004) 1759–1761.
[44] H. Wang, Z. Xu, G. Eres, Order in vertically aligned carbon nanotube arrays, Appl. Phys. Lett. 88 (21) (2006) 1105.
[45] A.C. Ferrari, J. Robertson, Interpretation of Raman spectra of disordered and amorphous carbon, Phys. Rev. B 61 (20) (1999) 14095–14107.
[46] S. Osswald, M. Havel, Y. Gogotsi, Monitoring oxidation of multiwalled carbon nanotubes by Raman spectroscopy, J. Raman Spectrosc. 38 (6) (2007) 728–736.
[47] M.S. Strano, C.A. Dyke, M.L. Usrey, P.W. Barone, M.J. Allen, H.W. Shan, C. Kittrell, R.H. Hauge, J.M. Tour, R.E. Smalley, Electronic structure control of single-walled carbon nanotube functionalization, Science 301 (5639) (2003) 1519–1522.
[48] M.S. Dresselhaus, A. Jorio, M. Hofmann, G. Dresselhaus, R. Saito, Perspectives on carbon nanotubes and graphene Raman spectroscopy, Nano Lett. 10 (2010) 751–758.
[49] Y.S. Xie, P.Y. Yuan, T.Y. Wang, N. Hashemi, X.W. Wang, Switch on the high thermal conductivity of graphene paper, Nanoscale 8 (40) (2016) 17581–17597.
[50] Z. Cheng, L.J. Liu, S. Xu, M. Lu, X.W. Wang, Temperature dependence of electrical and thermal conduction in single silver nanowire, Sci. Rep. 5 (2015) 10718.
[51] W. Zhou, J. Vavro, C. Guthy, K.I. Winey, J.E. Fischer, L.M. Ericson, S. Ramesh, R. Saini, V.A. Davis, C. Kittrell, M. Pasquali, R.H. Hauge, R.E. Smalley, Single wall carbon nanotube fibers extruded from super-acid suspensions: preferred orientation, electrical, and thermal transport, J. Appl. Phys. 95 (2) (2004) 649–655.
[52] M.C. Llaguno, J. Hone, A.T. Johnson, J.E. Fischer, Thermal conductivity of single wall carbon nanotubes: diameter and annealing dependence, Electron. Prop. Mol. Nanostruct. 591 (2001) 384–387.
[53] N. Matsumoto, A. Oshima, G.H. Chen, M. Yudasaka, M. Yumura, K. Hata, D.N. Futaba, Elucidating the effect of heating induced structural change on electrical and thermal property improvement of single wall carbon nanotube, Carbon 87 (2015) 239–245.
[54] J.A. Lenz, C.A. Perottoni, N.M. Balzaretti, J.A.H. da Jornada, Processing of amorphous carbon films by ultrafast temperature treatment in a confined geometry, J. Appl. Phys. 89 (12) (2001) 8284–8290.
[55] W.S. Bacsa, J.S. Lannin, D.L. Pappas, J.J. Cuomo, Raman-scattering of laser-deposited amorphous-carbon, Phys. Rev. B 47 (16) (1993) 10931–10934.
[56] A. Ferrari, J. Robertson, Raman spectroscopy of amorphous, nanostructured, diamond-like carbon, and nanodiamond, Phil. Trans. 362 (1824) (2004) 2477–2512.
[57] F. Tuinstra, J.L. Koenig, Raman spectrum of graphite, J. Chem. Phys. 53 (1970) 1126–1130.
[58] G. Barnes, D. Dewhughes, M. Mcculloch, Finite difference modelling of bulk high temperature superconducting cylindrical hysteresis machines, Supercond. Sci. Technol. 13 (2) (2000) 229.
[59] X. Liu, Z. Zou, S. Qu, J. Yao, Finite difference modeling on the temperature field of substrate in friction surfacing, J. Mater. Process. Technol. 209 (3) (2009) 1392–1399.
[60] F. Incropera, D. Dewitt, Fundamentals of Heat and Mass Transfer, 5 ed., Wiley, New York, 2002.
[61] R. Weast, Handbook of Chemistry and Physics, CRC, Boca Raton, Florida, 1983.
[62] K. Mizuno, J. Ishii, H. Kishida, Y. Hayamizu, S. Yasuda, D.N. Futaba, M. Yumura, K. Hata, A black body absorber from vertically aligned single-walled carbon nanotubes, Proc. Natl. Acad. Sci. U.S.A. 106 (15) (2009) 6044–6047.
[63] X. Wang, X. Xu, Thermal conductivity of nanoparticle–fluid mixture, J. Thermophys. Heat Tran. 13 (4) (1999) 474–480.
[64] M.M. Bernal, M. Tortello, S. Colonna, G. Saracco, A. Fina, Thermally and Electrically Conductive Nanopapers from Reduced Graphene Oxide: effect of nanoflakes thermal annealing on the film structure and properties, Nanomaterials 7 (12) (2017) 428.
[65] P.U. Jepsen, B.M. Fischer, A. Thoman, H. Helm, J.Y. Suh, R. Lopez, R.F. Haglund, Metal-insulator phase transition in a VO_2 thin film observed with terahertz spectroscopy, Phys. Rev. B 74 (20) (2006) 3840–3845.
[66] W. Desorbo, W.W. Tyler, The specific heat of graphite from 13-degrees-K to 300-degrees-K, J. Chem. Phys. 21 (10) (1953) 1660–1663.
[67] C.H. Deng, Y.M. Sun, L.J. Pan, T.Y. Wang, Y.S. Xie, J. Liu, B.W. Zhu, X.W. Wang, Thermal diffusivity of a single carbon nanocoil: uncovering the correlation with temperature and domain size, ACS Nano 10 (10) (2016) 9710–9719.
[68] K. Zhang, G. Stocks, J. Zhong, Melting and premelting of carbon nanotubes, Nanotechnology 18 (28) (2007) 285703.